First beam test of an additively manufactured H-mode linac structure made from pure copper

Hendrik Hähnel,[1,*] Philipp Müller,[1] Jan Dominik Kaiser,[1] Adem Ateş,[1] Leonie Bauer,[1] Benjamin Dedić,[1] Ulrich Ratzinger,[1] Patrick Reichart,[2] Günther Dollinger,[2] and Michael Mayerhofer[2]

[1]*Institute of Applied Physics (IAP), Goethe-Universität Frankfurt, 60438, Frankfurt am Main, Germany*
[2]*Institute for Applied Physics and Measurement Technology, University of the Bundeswehr Munich, Neubiberg, Germany*

(Received 7 November 2025; accepted 2 April 2026; published 5 June 2026)

This paper presents a high-power beam test of the first IH-type linac structure additively manufactured from pure copper performed in May 2025. The 433 MHz cavity with a total length of 20 cm has been tested up to 25 kW at a duty cycle of 2%, which corresponds to a cavity voltage of 0.86 MV with peak fields at the drift tubes reaching up to 68 MV/m without rf breakdown at full power. A 1.4 MeV proton beam from a Van de Graaff accelerator has been accelerated up to 2.212 MeV, demonstrating the effective acceleration voltage of 0.817 MV at full power. These high-power beam tests show performance on par with conventionally manufactured H-mode structures, paving the way for future linac structures benefiting from the advantages of additive manufacturing.

DOI: 10.1103/6fp9-dfyk

I. INTRODUCTION

Additive manufacturing (AM) of metals, and especially pure copper, has seen significant improvements in material density and overall quality of the parts produced in recent years due to significant improvements in technology both using red and green laser systems [1–3].

In 2020, the ADDLINAC[1] project was started at Goethe University Frankfurt to provide a proof of concept for additively manufactured linac structures from stainless steel and pure copper [4,5]. After first positive results with AM structures from stainless steel 316L, new technology using green lasers (TRUMPF TruPrint 5000, 500 W green fiber laser) allowed for the production of parts larger than 100 mm from pure copper. Due to its high thermal conductivity and the possibility of integrating surface-near cooling structures, AM copper is especially promising for high-power linac designs. To test the viability of copper AM parts for linear accelerator structures, a set of IH-type drift-tube structures from pure copper was produced in early 2023 (Fig. 1). These structures have been extensively tested in a demonstrator cavity, culminating in successful beam tests in 2025.

In recent years, a number of studies on the topic of AM for linear accelerator components have been published [6]. Efforts can roughly be divided into structures from stainless steel that need to be copper plated after manufacturing and pure copper structures that, with careful surface preparation, could be used directly for linac structures. First examples of practical applications of stainless steel AM manufacturing in H-mode cavities are the first coupled CH cavity (CCH) for the FAIR proton linac and the IH-type

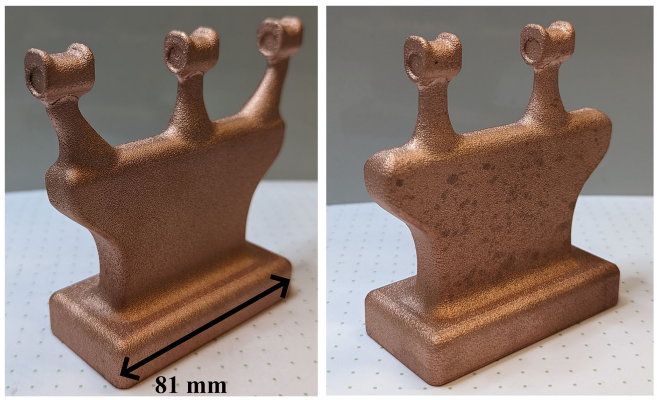


FIG. 1. Copper AM girders after printing before postprocessing. Drift tubes are filled solid to be drilled out and the bottom has been produced with excess material for CNC machining of the sealing surfaces.

*Contact author: haehnel@iap.uni-frankfurt.de

[1]Additive Manufacturing of Linear Accelerators.

Published by the American Physical Society under the terms of the Creative Commons Attribution 4.0 International license. Further distribution of this work must maintain attribution to the author(s) and the published article's title, journal citation, and DOI.

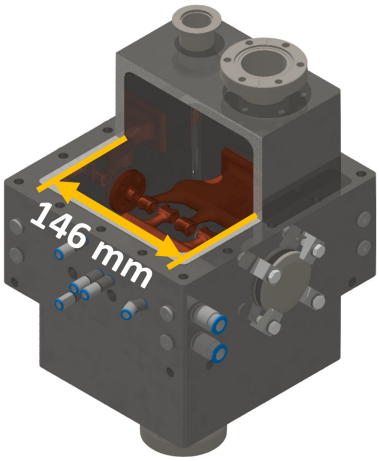


FIG. 2. CAD cross section of the AM IH-DTL cavity prototype. The cavity frame and lids are made from stainless steel and copper plated. Several CF and KF ports are attached to the cavity for flexibility in attaching diagnostics.

KoBRA buncher cavity. For the FAIR CCH, the crossbar stems with drift tubes were made from AM stainless steel for easy implementation of cooling channels in the drift tubes. Electron beam welding of the AM crossbars was demonstrated successfully [7,8]. The KoBRA buncher IH-type cavity also has AM stainless steel stems and drift tubes and has already been commissioned with beam at RAON in 2024 [9,10]. For both applications, the AM stainless steel parts are CNC machined and copper plated afterward.

The topic of pure copper linac structures is under investigation by several groups around the world. Examples include a 750 MHz RFQ (I.FAST) [11], as well as studies for higher frequency structures at S band, X band, and other frequencies [12–15]. The inherent surface roughness of AM parts leads to significant reduction in rf conductivity in the as-built condition [16,17]. This can be addressed by remachining and/or surface polishing. Therefore, especially for pure copper structures, the topics of surface postprocessing [18–21], powder quality, and process parameters during the AM process [22,23] are much more prominent due to the direct exposure of these surfaces to the rf fields in the cavities.

II. CAVITY DESIGN

The cavity is based on the interdigital H-mode structure (IH-DTL) which is an efficient structure for hadron beams between 0.02 and 0.2 c with typically high shunt impedances between 50 and 300 MΩ/m [24–28]. This cavity was designed for a resonance frequency of 433.632 MHz with a total of six acceleration gaps (see Fig. 2). It is the highest frequency IH-DTL used for beam acceleration to date. The beam dynamics and cavity rf parameters are summarized in Table I.

TABLE I. Mechanical and rf parameters of the AM IH-DTL prototype cavity for the beam test.

General parameters	Design
Resonance frequency: f_{res}	433.632 MHz
Outer dimensions (w/h):	221/261 mm
Outer length: L_{outer}	206 mm
Inner length: L_{inner}	146 mm
Period length ($\beta\lambda/2$): L_p	19–24 mm
Reference particle:	Proton
Initial energy: W_{in}	1.4 MeV
Final energy: W_f	2.4 MeV
Simulations at beam test frequency	*Simulation*
Resonance frequency: f_{res}	439.6 MHz
Unloaded Q-factor: Q_0	8603
Cavity rf losses:	25 kW
Cavity voltage: V_0	1.08 MV
Effective shunt impedance: Z_{eff}	234 MΩ/m
Measurements at frequency	*Measurement*
Resonance frequency: f_{res}	439.6 MHz
Unloaded Q-factor: Q_0	6836
Cavity rf losses:	25 kW
Cavity voltage: V_0	0.86 MV
Effective shunt impedance: Z_{eff}	186 MΩ/m

A. Beam dynamics design

To ensure high-energy gain for the 1.4 MeV synchronous particle, the beam dynamics design was chosen to be similar to a zero-degree section of a typical KONUS lattice [29] with a mean synchronous phase of $\phi_s = 10°$, starting at an excess energy of $W_{\mathrm{bc}} = 6.5\%$. This way, the bunch can stay close to $\phi_s = 10°$ for more gaps. During the beam test, the bunch motion with the highest energy gain will shift from $\phi = -7.3°$ to $\phi = +7.3°$ relative to the synchronous particle of the gap structure, leading to a final energy of 2.212 MeV. Cluster plots for the longitudinal bunch motion are shown in Fig. 3. The beam dynamics design was simulated with LORASR [30,31] while all further simulations were done with TraceWin [32] using a 3D electromagnetic fieldmap of the cavity to get the best agreement between the beam test data and tracking simulations (see Sec. IV A).

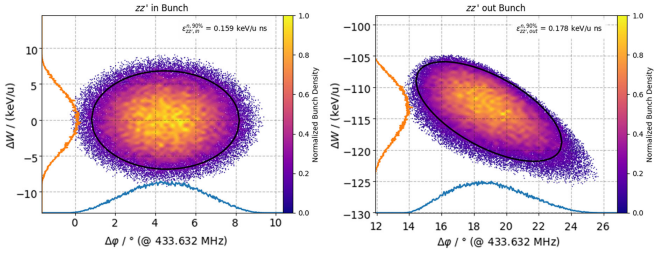


FIG. 3. Cluster plot of the longitudinal bunch at the entrance of the cavity (left) and at the exit after acceleration with an effective voltage of 0.817 MV corresponding to the beam experiments at 25 kW.

B. Resonator design

Design and simulation of the cavity rf were performed in CST Microwave Studio using the eigenmode solver [33]. The primary design objectives were high shunt impedance, effective dipole compensation, and compatibility with a modulator design for the AM drift-tube structures. A small aperture of 7 mm in diameter was chosen as a compromise between beam acceptance and shunt impedance. A slim drift-tube and girder design, along with further geometry optimization, lead to an effective shunt impedance of $Z_{\mathrm{eff}} = 253\ \mathrm{M\Omega/m}$ simulated for the latest girder revision used in the beam test. The unloaded quality factor Q_0 is simulated to be 8808. For the beam tests, an additional capacitive tuner was used to offset the frequency shift from material removal during polishing of the AM drift-tube structure (see Fig. 4). This version, as expected, is slightly less efficient with $Z_{\mathrm{eff}} = 234\ \mathrm{M\Omega/m}$ and $Q_0 = 8603$. These values will be used for comparison of power test and beam test data. Bead pull measurements of the cavity, as used in the beam tests, were performed with a 2.95 mm PTFE spherical bead and a Rohde & Schwarz ZNB4 vector network analyzer. The measured field distribution on axis is compared to a simulation of the cavity performed in CST Microwave Studio (see Fig. 5). A total of 20 measurements were averaged showing a maximum deviation of the gap voltages between −0.86% and + 2.1% with an average deviation of 0.75% (absolute values).

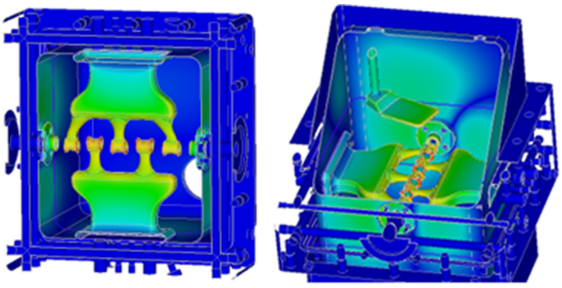


FIG. 4. Electric field simulated for the cavity in ideal conditions (left) and with an additional capacitive tuner, as used in the beam tests (right).

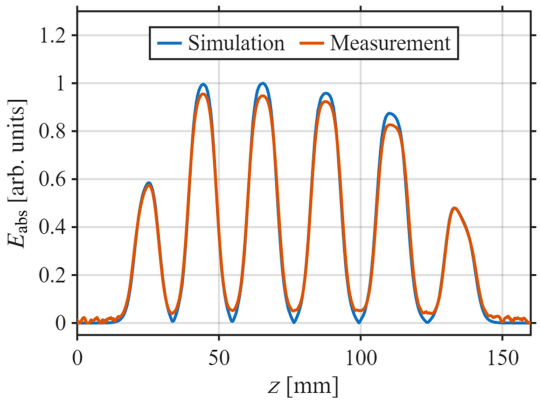


FIG. 5. Comparison of the on-axis field distribution simulated with CST Microwave Studio with bead-pull measurements of the AM-IH-DTL with the final copper AM girders installed. After baseline correction of the measured data, both curves are normalized to the same total area.

C. Mechanical design

The cavity was built with modularity in mind to allow testing of multiple iterations of the AM drift-tube structures. The stainless steel cavity lids and the center frame have been conventionally manufactured by CNC machining. The drift-tube structures are mounted in rectangular recesses in the cavity's middle frame. These recesses have been produced to a fit tolerance of 100 μm by die-sinking EDM, as machining the pockets was not feasible due to space constraints within the frame. The center frame is surrounded by cooling channels, as well as through connections to the drift-tube structure water cooling channels. The lids are not water cooled, as the power load on each lid is only about 5%. The internal water cooling channels of the girders are shown in Fig. 6. Cooling is achieved with parallel cooling channels for each stem, which reach up to the drift tubes. Cooling channel diameters are 2.8 mm to ensure about 1 mm of wall thickness at the stems. Water connections at the drift-tube structures are done using Festo QSM fittings to fit the small footprint. This setup has proven to be sufficient for the operation at 25 kW with a duty cycle of 2%, which corresponds to an average thermal load of 500 W. Further improvements of the cooling structure for higher power are currently under investigation.

Cavity vacuum is achieved by a combination of 1.5 mm soft-annealed aluminum wire as the main gasket and additional O-rings behind the wire so that the space in between can be evacuated. This way, if during extended operation the aluminum gasket should partially fail, leak rates could be reduced to manageable levels, ensuring continuation of operation. In all tests so far, the additional vacuum was not needed as the aluminum gaskets on the lids and the drift-tube structures were sufficient. For high-power tests, the main gasket on the foot of the AM drift-tube structures consisted of a combination of aluminum wire as rf contact and an O-ring as vacuum gasket. This accounts

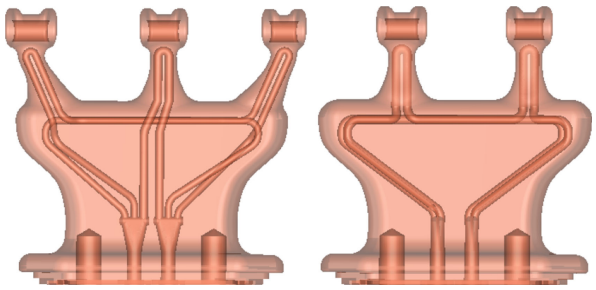


FIG. 6. View of the AM drift-tube structures with cooling channels in the stems.

for the fact that the structures were annealed at 400 °C after CNC machining and were therefore relatively soft and prone to deformation under excessive mechanical load. Cavity vacuum for the beam tests was typically in the range of 2×10^{-7} to 4×10^{-7} mbar without rf (compare [34,35]).

D. Printed parts and their preparation

To date, three different revisions of the drift-tube structure have been designed and printed from stainless steel and finally pure copper. The current revision features cooling channels running through the girder and up to just below the drift tubes. The AM copper parts were produced on a TRUMPF TruPrint 5000 Green Edition, which has a 800 W green laser (515 nm). AM copper parts after manufacturing have a surface roughness on the order of $R_z = 15$–30 μm. Therefore, for first tests with these structures, the contour of the parts was CNC machined to remove 200 μm from all surfaces, providing a near mirror finish on the flat sides while leaving some rough spots where milling did not reach full depth. These rough spots were the main source of field emission in previous power tests [34].

After these first power tests in 2024, the original AM copper girders were additionally manually polished until the whole surface had a near mirror finish. As a result, no field emission was detected in subsequent power tests. The resulting polished surfaces can be seen in Fig. 7. Due to further material removal from polishing, the cavity resonance frequency increased to about 441 MHz. This frequency increase is consistent with an average surface removal of 257 μm from CNC machining and subsequent polishing. For beam tests, the resulting frequency shift was partially compensated with a capacitive tuner with minimal impact on the cavity quality factor. In future structures, this deviation has to be taken into account, and sufficient tolerances have to be included in the print models.

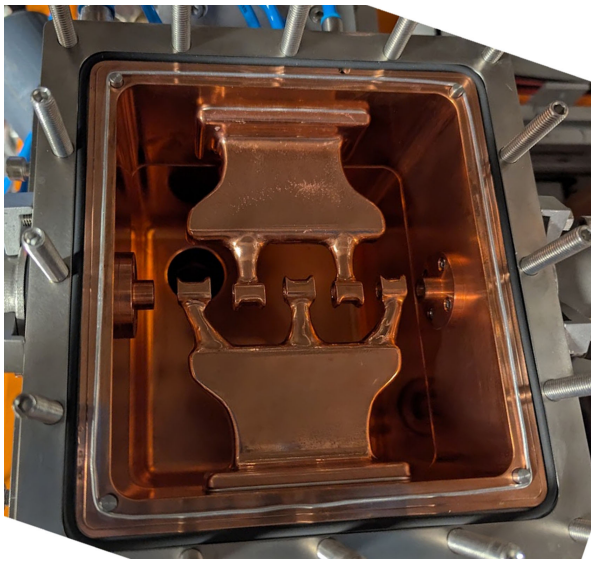


FIG. 7. AM IH-DTL with the polished copper AM girders mounted for operation.

III. EXPERIMENTAL SETUP

The experiment was set up at the Institute of Atomic Physics at Goethe University Frankfurt. There, a 2.5 MV Van de Graaff accelerator was used to produce a 1.40 MeV proton beam to be accelerated by the AM-IH cavity. The cavity is driven by a pulsed solid-state amplifier, and the proton energy spectrum is measured about 1.7 m behind the cavity using a Si-PIN diode. The setup will be described in detail in the following sections.

A. Amplifier and rf setup

The main rf amplifier is a 433 MHz solid-state amplifier by BONN Elektronik (with a broad bandwidth of at least ±10 MHz), providing up to 26 kW for 2 ms pulses at a repetition rate of 10 Hz. The amplifier is connected to the cavity with EIA 3 1/8 in. rigid coaxial transmission line, including a bidirectional coupler for measurement of forward and reflected power. Behind the bidirectional coupler, the coaxial line size is reduced to EIA 1 5/8 in. for easier handling and connection to the compact coupler.

An rf pickup in the top lid of the cavity is used to measure transmitted power by weak capacitive coupling. The pickup was measured with a transmission of $S_{21} = -50.31$ dB. The cavity was tuned to 439.6 MHz for the power tests and beam tests reported here. This frequency was chosen to minimize impact on the cavity acceleration performance while keeping thermal load on the tuner as low as possible to ensure stable operation. The cavity was operated at a repetition rate of 10 Hz both for high-power tests and for beam tests with a pulse length of 2 ms. The cavity rf signal was linearly ramped at the rising and falling edge with ramp times between 28 and 140 μs. Low-level rf control is provided by in-house custom-built hardware, which allows for flexible configuration and implementation of new features [36]. Amplitude control can be performed for forward, reflected, and transmitted power, giving flexibility to the operator, especially useful at low-power conditioning scenarios. Additionally, a dynamic vacuum-pressure-based amplitude limiter, as well as a trip limiter capable of < 10 μs shutoff in case of total reflection, is implemented in hardware. Additional power meters (Rohde & Schwarz NRX) are used for cross-check of forward, reflected, and transmitted power. Data acquisition is performed using a custom control system based on the meshed networked data acquisition and control system which was also developed in-house [37].

Due to the small dimensions of the cavity, the largest flange size available for rf coupling is CF40. Therefore, a compact rf coupler had to be developed for the high-power rf tests. A fully optimized coupling loop made by AM of

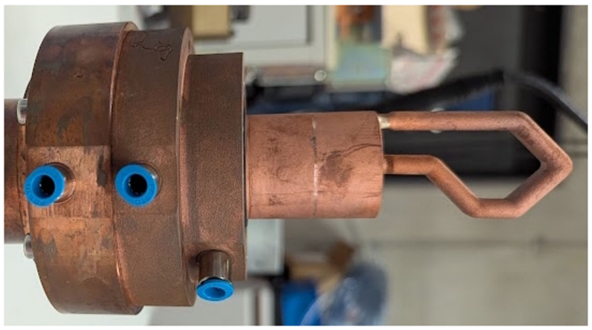


FIG. 8. Fully AM compact CF40 rf coupler used for high-power tests and beam experiments.

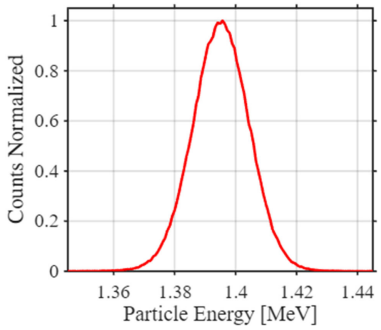


FIG. 10. Measured Gaussian energy spectrum of the tuned Van de Graaff beam used for beam tests.

pure copper was developed and successfully employed for the following power tests in 2025 (see Fig. 8).

This optimized coupler consistently showed critical matching with reflected power below $S_{11} \leq -30$ dB in low-level rf measurements (using a vector network analyzer), as well as during high-power operation. The coupling loop was measured at $S_{11} \leq -35.4$ dB for the cavity tuned to 439.6 MHz as it was used in high-power tests and beam tests. A detailed description of the coupler design and performance can be found in [38].

B. Beamline setup

The cavity was set up on the neutron production beamline at the 2.5 MV Van de Graaff accelerator situated at the Institute of Atomic Physics (IKF), Goethe University Frankfurt. The cavity was positioned downstream of the analyzing dipole. A set of x/y collimating slits in front of the cavity was used in combination with a circular 1 mm diameter pinhole aperture directly in front of the cavity entrance to provide an aligned pencil beam to the cavity with sufficiently low intensity to prevent detector saturation (Fig. 9). Energy measurements were performed with a Si-PIN diode detector at a distance of 1.7 m behind the cavity (with another 10 mm circular orifice in front of the detector). The cavity and detector were aligned to the beam axis of the Van de Graaff accelerator using a Taylor Hobson telescope mounted at the end of the beamline. The beam was aligned using the detector signal to find the center of mass of the Van de Graaff accelerator beam by scanning the beam in both horizontal and vertical directions to find the highest intensity. This was also necessary to obtain a clean Gaussian profile of the Van de Graaff accelerator beam at the pinhole entrance (see Fig. 10). Beam fractions from the fringes of the beam would have a high fraction of refracted protons with lower energies, producing a tail of low-energy particles broadening the beam energy spectrum.

C. Proton energy detection

For analysis of the proton energy behind the cavity, we use Si-PIN diodes (type SFH946, Siemens) with an active area of 10×10 mm mounted on a simple holder on a KF40 vacuum flange to fit directly into the center of the beam axis. The depletion layer thickness of 380 μm is sufficient to stop up to 7 MeV protons (range calculation from [39,40]). The PIN-structure surface is aluminized at the front (1.4 μm) and covered by a 0.2 μm thick Si_3N_4 passivation layer. The pulse signal is read out by a charge-sensitive preamplifier (Mesytec MPR-1) and processed by a standard ORTEC 570 shaping amplifier (0.5 μs shaping time). We use a VME-Bus ADC (Mesytec MADC-32) to record the pulse height as an energy value for each proton and collect and analyze the data by a Mesytec MVLC module together with the open source Mesytec MVME software on a standard Windows PC [41].

We tested the PIN diodes under ideal lab conditions with a standard mixed nuclide alpha source. The energy resolution for 5.5 MeV alpha particles was found to be about 0.7% (38 keV) FWHM to demonstrate sufficient accuracy for the beam energy analysis. In the special electronic environment of the beam line with the potential rf noise of the rf cavity in close distance to the detector, the energy resolution was tested directly with the energy calibrated

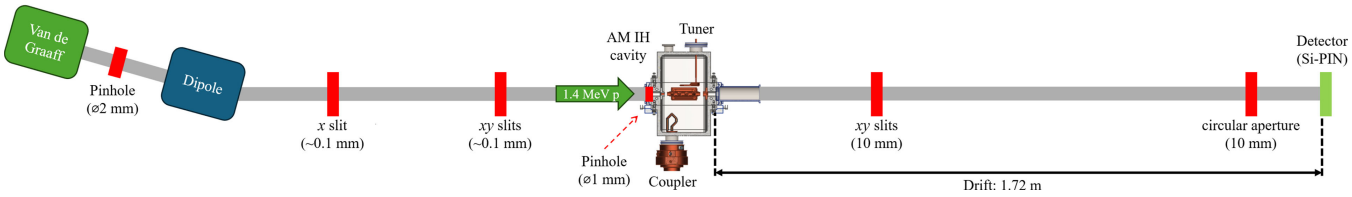


FIG. 9. Layout of the beamline used for beam tests (not to scale). A combination of slits and pinholes in front of the cavity was used to produce the pencil beam for beam tests. Slits and the aperture behind the cavity were kept open.

1.4 MeV proton beam and found to be 20 and 23 keV for two different Si-PIN diodes which includes 2 keV beam energy spread and corresponds to a relative energy resolution of about 1.5% FWHM. Final calibration of the detector used for the cavity beam tests was performed using a linear fit ($R^2 = 0.99998$), correlating the detector bins to the known beam energy of the Van de Graaff accelerator in the range between 0.8 and 2.3 MeV (which was considered to be accurate within ±2 keV, see Sec. IV).

The beam current was reduced by slit pairs in front of the cavity to a count rate of a few kHz on the PIN diode in order to prevent the PIN diode from beam damage as well as pile up events in the energy spectrum and to keep the dead time of the data acquisition at a reasonable level.

The data acquisition was time-gated so that the measurement data were only collected in coincidence with the cavity rf pulse. To prevent any signal from the unaccelerated Van de Graaff beam, the time gate signal was produced by taking the cavity rf pulse and offsetting the gate signal by +250 μs from the rising edge and −100 μs from the falling edge with a Stanford Research DG535 delay generator.

D. Cavity conditioning

Conditioning for the beam tests was done solely with the BONN Elektronik amplifier at a duty cycle of 2%. Multipacting was observed at similar power levels as previously up to several hundred watts, and at a range of 3–5 kW [34]. Multipacting around 8–9 kW was absent during this conditioning run, which might be due to the replacement of the rf coupler for this power test. No significant breakdown or field emission was observed during high-power conditioning.

Since the amplifier saturated at around 26 kW, stable operation of the cavity at a forward power of $P_F = 25$ kW was possible at full 2% duty cycle (2 ms, 10 Hz). During high-power conditioning, the transmitted power increased in subsequent sessions from $P_T = 22.9$ kW up to a final value of $P_T = 25$ kW coinciding with the forward power. Reflected power was consistently around $P_R = 28$ W at full power after conditioning. Cavity performance has been significantly increased from the first power tests in 2024 to full-power operation in 2025. This is mainly due to improved surface quality of the AM parts. Surface fields

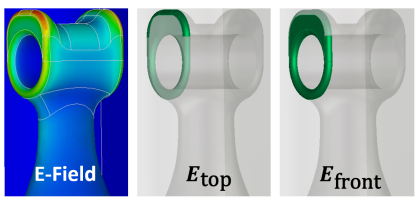


FIG. 11. Electric field distribution on the drift tubes (left), drift-tube areas for the top (highest fields) and front of the drift tubes are marked in green (middle and right, respectively).

TABLE II. Surface and gap electric fields for the cavity power test (see Fig. 11). Simulated values for 25 kW cavity power, as well as values achieved at the power test in 2025 are shown (scaled based on the measured Q_0 of the cavity).

	E_{front} [MV/m]	E_{top} [MV/m]	E_{axis} [MV/m]	V_0 [MV]
25 kW	(mean/max)		(linac/gap)	
CST	41.7/63	71.1/85.1	7.39/18.5	1.08
Power test	33.1/50.1	56.5/67.6	5.87/14.7	0.86

of $33 - 56$ MV/m with peak values of up to 68 MV/m were reached on the drift tube front and top surfaces, respectively (see Fig. 11 and Table II).

IV. BEAM TESTS

The beam tests were performed with a 1.40(2) MeV proton beam with Gaussian energy distribution (FWHM between 20.5 and 23.7 keV). The energy calibration of the Van de Graaff accelerator was known to be accurate within ±2 keV from neutron activation experiments on the same beamline, where a calibration based on a $Al(p,\gamma)$ reaction was performed [42]. Measurements were performed at different power levels of $P_f \in \{1, 5, 10, 15, 20, 25\}$ kW to evaluate the acceleration performance of the cavity. Amplitude control was enabled to keep forward and transmitted power constant over the duration of the measurement. The Van de Graaff beam current to the cavity was adjusted to be low enough to prevent event pileup in the detector. The total amount of pileup events in the measurements was below 0.001% of the measured counts and is therefore considered insignificant. Pileups were mostly caused by random current fluctuations of the Van de Graaff accelerator beam. Measurements were performed until at least 40,000 counts were reached. The measurement time needed to be increased from about half an hour at lower power levels to almost 2 h at full power due to the increased divergence of the beam at higher power levels.

A. Cavity response predictions

Since the Van de Graaff beam is continuous and the cavity is operating with a rf frequency of 439.6 MHz, the measurement basically amounts to a time-integrated phase scan of the cavity [43]. This means that some protons will be accelerated at the full cavity effective acceleration voltage, while the rest will be accelerated less and even decelerated. To predict the cavity response, 3D electromagnetic fieldmaps of the cavity were used to track particles through the cavity at various power levels in TraceWin. The cavity field was scaled according to the measured Q_0 of the cavity to simulate actual field levels in the cavity during measurement. The simulation starts with a pencil beam (as enforced by the pinhole in front of

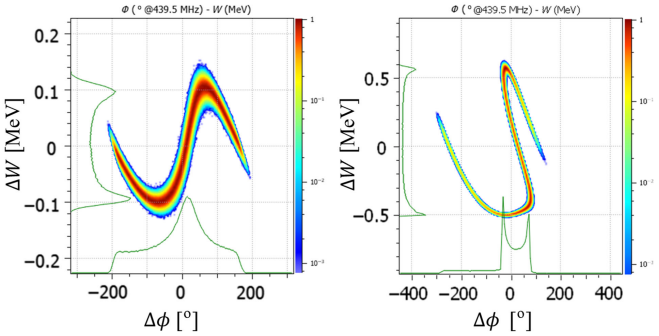


FIG. 12. Longitudinal particle distribution directly behind the cavity (TraceWin fieldmap simulation) for 1 kW (left) and 25 kW (right). Normalized particle density is shown on a logarithmic color scale.

the cavity) with an rms energy width of 9 keV which corresponds to an FWHM of 21 keV for the Gaussian beam of the Van de Graaff accelerator. A 4D Gaussian particle distribution (3σ truncated) was used as the input distribution. While the energy spectrum of the beam was measured to be Gaussian, the exact transverse distribution is not known but can be reasonably approximated as Gaussian as well. Examples for cavity responses at 1 and 25 kW are shown in cluster plots in Fig. 12 directly behind the cavity and Fig. 13 at the detector position. The longitudinal particle distribution at 1 kW is mostly consistent with a sinelike energy modulation showing a full rf cycle of the cavity. The distribution at full power looks less predictable. This is to be expected, as at lower power levels, the particle velocity change is much lower. At higher power, the change in particle velocity leads to more significant phase shift and therefore more irregular particle motion for particle phases further from the synchronous particle.

As mentioned before, the part of the beam that has interacted with cavity fields has an increasingly high divergence, especially for the lower energy particles due to their asynchronous motion in the cavity. As can be seen in Fig. 14, there is a significant increase in transverse

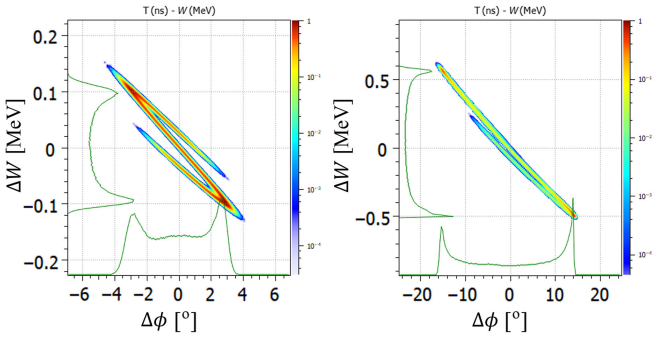


FIG. 13. Longitudinal particle distribution at the detector position after a 1.72 m drift (TraceWin fieldmap simulation) for 1 kW (left) and 25 kW (right). Normalized particle density is shown on a logarithmic color scale.

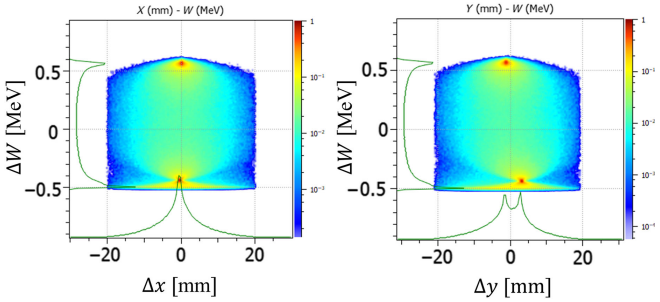


FIG. 14. Particle distribution plotting particle energy relative to particle vertical and horizontal position at the detector at 25 kW. In the vertical plane, a slight displacement of the high-energy particles as well as a more significant displacement of the low-energy particles can be seen caused by residual cavity dipole field components. Normalized particle density is shown on a logarithmic color scale.

particle positions after the drift to the detector in the medium-energy range of the bunch. The center of mass of the lowest energy particles is offset by as much as 3.1 mm corresponding to a deflection angle of 1.8 mrad in the vertical plane. This was confirmed by experiments using a 3 mm diameter circular aperture placed in front of the detector, where the low-energy peak in the measured spectrum disappeared. The displacement is due to the dipole field component of the cavity, which for nonsynchronous particles leads to significant deflection behind the cavity. High-energy particles, which are synchronous with the cavity gap structure, experience significantly small deflection of around −0.7 mrad (the simulated residual dipole field is 1.7% of E_z on axis). In the horizontal plane, the beam is not displaced, as the dipole components act only in the plane of the girders and drift tubes.

Finally, the expected energy distribution can be extracted from TraceWin simulations by creating an energy histogram of the cluster data. For the simulations, 10^6 macroparticles were used. The cluster data were then divided into 5 keV wide bins. The resulting energy spectra for cavity rf power in the range of 1–25 kW are shown in Fig. 15. For these evaluations, only particles within the 10×10 mm^2 area of the detector are considered. At 25 kW, a final beam energy of 2.182 MeV is predicted by the simulations, corresponding to an energy gain of 782 keV.

B. Beam energy measurement results

Several measurement campaigns were performed at the Van de Graaff beamline in 2025 to obtain reliable beam energy measurements of the AM-IH-DTL. The rf forward power was used as the reference for all plots because even though the pickup has been carefully calibrated, signals from the bidirectional coupler are more reliable. Once the cavity was fully conditioned, deviation of transmitted power from forward power, however, was minimal. As can be seen from Fig. 16, the measured energy spectra

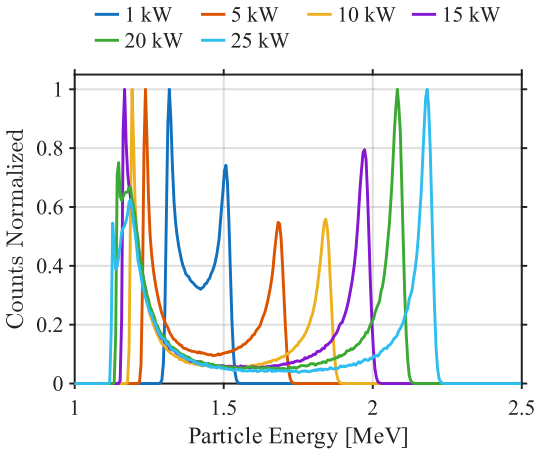


FIG. 15. Energy distribution of proton beams at the detector position calculated from TraceWin simulations for the different power levels. For improved visibility, the spectra are normalized to their highest peaks.

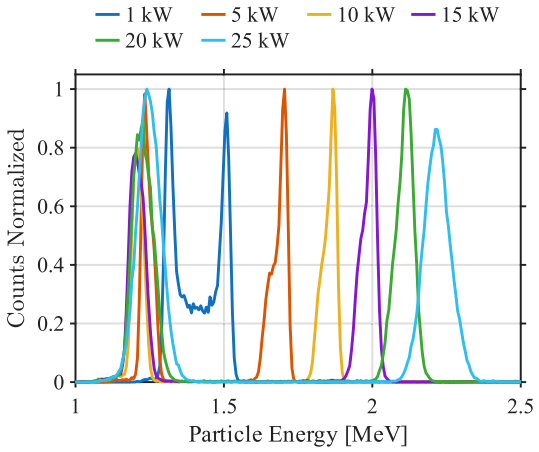


FIG. 16. Energy distribution of proton beams measured by the Si-PIN detector after acceleration in the cavity for the different forward power levels.

overall agree with the predictions from beam dynamics simulations. Some notable differences are the higher FWHM of higher power measurements as well as a vanishing of intermediate energies at and above 5 kW. The higher overall width for 20 and 25 kW is most likely due to variations in forward power during these measurements. The energy width of the Van de Graaff beam stayed constant throughout all measurements. The intermediate particle energies can be clearly seen at 1 kW, where the measured particle spectrum is very close to the simulations. At higher power, a combination of lower count rates and increased beam divergence after the cavity is suspected to be a contributing factor to lower signals at intermediate energies. As shown in Fig. 14, the highest and lowest energy particles are concentrated around the beam axis, whereas intermediate particle energies show a much wider transverse spread at the detector. In case that the beam does not hit the detector perfectly in the center of the active area, parts of the intermediate energy spectrum are cut off to a higher degree than the peaks at both ends of the spectrum.

The detector data provide a total of 8192 bins with a width of 0.8 keV. Total count rate was around 40,000 for all measurements except at 25 kW, where a total of 100,000 counts was measured. To improve the data quality and reduce fluctuations, the data were rebinned by a factor of 8, resulting in a bin width of 6.3 keV for the final spectra. All results from the beam energy measurements are summarized in Table III. At a final power of 25 kW, a beam energy of 2.212 MeV was measured, which corresponds to an energy gain of 817 keV, which is 35 keV higher than predicted by beam dynamics.

A comparison of all measured energies and the simulation data is shown in Fig. 17. The measured energies are consistently slightly higher than predicted by the simulations, while the overall trend closely follows the simulations. This is further confirmation that the simulation and measurement agree well and minor differences can be attributed to scaling of the fieldmaps, deviations of the actual cavity fields from simulation, and uncertainties in the precise measurement of transmitted power to the cavity.

C. Cavity shunt impedance and effective voltage

The shunt impedance of a linac cavity can be determined in multiple ways. A comparison of the measured and simulated unloaded quality factor Q_0 (from CST eigenmode

TABLE III. Measurement results from beam tests of the AM IH-DTL with a 1.4 MeV Van de Graaff beam. Peak energies correspond to Fig. 16.

P_{fwd}[kW]	P_{ret}[W]	W_{VdG}[MeV]	W_{min}[MeV]	W_{max}[MeV]	$W_{\mathrm{max}} - W_{\mathrm{VdG}} = \Delta W_{\mathrm{accel}}$[keV]
1	2	1.394	1.315	1.510	115
5	7	1.394	1.234	1.704	310
10	9	1.391	1.209	1.867	473
15	15	1.396	1.202	1.999	603
20	30	1.396	1.228	2.112	716
25	31	1.396	1.240	2.212	817

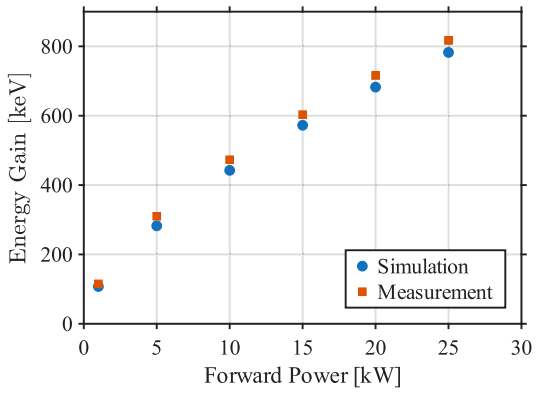


FIG. 17. Comparison of simulated and measured energy gain for 1.4 MeV protons after acceleration in the AM-IH-type structure. Measured energies are slightly higher than the simulated values.

simulations) yields a good approximation of the actual effective shunt impedance of the cavity Z_{eff} by

$$Z_{\mathrm{eff,LLRF}} = \frac{Q_{0,\mathrm{meas}}}{Q_{0,\mathrm{sim}}} \cdot Z_{\mathrm{eff,CST}}. \tag{1}$$

This calculation assumes that the voltage distribution in the measured cavity is identical to the simulated voltage distribution. However, this assumption is supported by bead-pull measurements and therefore this approximation holds as long as the cavity is well adjusted. A more direct way to obtain an effective shunt impedance is to use the measured energy gain of the particle beam, which directly corresponds to the effective voltage experienced by the beam. The requirement for this to be accurate is that the particle travels synchronous to the intended beam dynamics of the cavity at $\phi = 0°$. With P_c as the cavity power, ΔW_{acc} the particle energy gain and L the effective inner cavity length, the measured effective shunt impedance is

$$Z_{\mathrm{eff,beam}} = \frac{(\frac{\Delta W_{\mathrm{acc}}}{e})^2}{P_c \cdot L}. \tag{2}$$

We can now calculate both values for the AM-IH-DTL cavity using data from the beam test. From low-level rf measurements using a Vector Network Analyzer, the measured unloaded quality factor of the cavity is known to be 6836 (Table I). With a simulated Q_0 of 8603 and a simulated $Z_{\mathrm{eff,sim}} = 234.3\ \mathrm{M\Omega/m}$, we get

$$Z_{\mathrm{eff,LLRF}} = 186.1 \pm 0.5\ \mathrm{M\Omega/m}. \tag{3}$$

From the beam test results, using the highest achieved beam energy of 2.212 MeV with $L = 0.146$ m, we get

$$Z_{\mathrm{eff,beam}} = 182.7 \pm 4.4\ \mathrm{M\Omega/m}. \tag{4}$$

While the energy measurement of the proton beam is considered to be the most accurate of the measured values, the measured rf power introduces a larger error contribution to this calculation. Within the confidence of the calculation, both Z_{eff} values agree well. The shunt impedance demonstrated here is on the high end for IH-type structures. It is 79.4% of the simulated effective shunt impedance, which can directly be attributed to the rf conductivity of the cavity. Similar to other IH-type structures, the AM-IH-DTL is constructed from a middle frame and lids as well as separately mounted girder drift-tube structures. At each interface, the rf contact ensured by soft aluminum wire gaskets, which introduces some amount of contact resistance reducing the overall conductivity of the cavity. This is one area where future AM structures can further improve linac performance, since monolithic structures or even a reduction of the number of interfaces could yield much closer to simulation level performance with Q/Q_{sim} above 90%.

V. SUMMARY AND CONCLUSIONS

In this experiment, we accelerated a 1.4 MeV proton beam to 2.2 MeV with an additively manufactured pure copper drift-tube structure, demonstrating the feasibility of AM for normal conducting linac cavities. Moreover, to our knowledge, this is the highest frequency IH-DTL that has been realized and applied for ion-beam acceleration to date. We show that, with proper surface preparation, unloaded quality factors comparable to those of conventionally manufactured IH-type cavities can be achieved using AM. The effective shunt impedance was measured to be 186 MΩ/m. AM linac structures can enable higher duty cycle operation due to the ease of integration of conformal cooling channels. Additionally, AM can provide significant reduction in production cost for highly complex linac structures with fully water-cooled geometries. This new technology allows for the realization of considerably smaller structure components, leading to higher rf frequencies.

ACKNOWLEDGMENTS

The authors would especially like to thank M. Schöffler, M. Dworak, and P. Ziel from IKF at Goethe University Frankfurt for their active support during the beam experiments at the IKF Van de Graaff accelerator. We would also like to thank the company TRUMPF for providing the AM copper structures used in the experiments. Furthermore, we would like to thank T. Dettinger, Technology Laboratory at GSI Darmstadt, for annealing of the copper AM structures. This work was supported by the German Federal Ministry of Education and Research (BMBF) under Grant No. 05P21RFRB2.

DATA AVAILABILITY

The data that support the findings of this article are not publicly available upon publication because it is not

technically feasible and/or the cost of preparing, depositing, and hosting the data would be prohibitive within the terms of this research project. The data are available from the authors upon reasonable request.

[1] V. Ho, L. Ladani, J. Razmi, S. Gruber, A. B. Murphy, C. Chen, D. East, and E. Lopez, Powder bed fabrication of copper: A comprehensive literature review, Metals **15**, 1114 (2025).

[2] M. S. Khandpur, A. Giubilini, L. Iuliano, and P. Minetola, On the use of green and blue laser sources for powder bed fusion: State of the art review for additive manufacturing of copper and its alloys, Metals **14**, 1464 (2024).

[3] T. De Terris, T. Baffie, and C. Ribière, Additive manufacturing of pure copper: A review and comparison of physical, microstructural, and mechanical properties of samples manufactured with laser-powder bed fusion (L-PBF), electron beam melting (EBM) and metal fused deposition modelling (MFDM) technologies, Int. J. Mater. Form. **16**, 32 (2023).

[4] H. Hähnel and U. Ratzinger, First 3D printed IH-type linac structure—Proof-of-concept for additive manufacturing of linac rf cavities, Instruments **6**, 9 (2022).

[5] H. Hähnel, A. Ateş, B. Dedić, and U. Ratzinger, Additive manufacturing of an IH-type linac structure from stainless steel and pure copper, Instruments **7**, 22 (2023).

[6] T. Romano, G. Pikurs, A. Ratkus, T. Torims, N. Delerue, M. Vretenar, L. Stepien, E. López, and M. Vedani, Metal additive manufacturing for particle accelerator applications, Phys. Rev. Accel. Beams **27**, 054801 (2024).

[7] A. Seibel, M. Breidt, T. Dettinger, J. Egly, H. Hähnel, C. Kleffner, K. Knie, U. Ratzinger, and C. Will, Welding and copper plating investigations on the FAIR proton linac, in *Proceedings of the 31st International Linear Accelerator Conference LINAC-2022, Liverpool, UK* (JACoW, Geneva, Switzerland, 2022), pp. 345–347, 10.18429/JACOW-LINAC2022-TUPOJO05.

[8] C. Kleffner, A. Schnase, A. Seibel, C. Muehle, C. Will, G. Schreiber, H. Hähnel, K. Knie, M. Rodionova, M. Vossberg, M. Schuett, P. Forck, R. Hettinger, S. Udrea, S. Puetz, T. Sieber, U. Ratzinger, and V. Srinivasan, Progress and status of the FAIR proton linac, in *Proceedings of the 32nd International Linear Accelerator Conference LINAC-2024, Chicago, IL* (JACoW, Geneva, Switzerland, 2024), pp. 387–389, 10.18429/JACOW-LINAC2024-TUPB026.

[9] H. Hoeltermann, U. Ratzinger, W. Schweizer, D. Strehl, M. Schwarz, H. Hähnel, K. Tshoo, C. Ham, D. Kwak, T. S. Shin, and D. Yoon, Technical design of an IH-type buncher for KoBRA at RAON, J. Korean Phys. Soc. **83**, 589 (2023).

[10] H. Höltermann (private communication).

[11] T. Torims, G. Pikurs, S. Gruber, M. Vretenar, A. Ratkus, M. Vedani, E. López, and F. Brückner, First proof-of-concept prototype of an additive manufactured radio frequency quadrupole, Instruments **5**, 35 (2021).

[12] C. Nantista, D. Gamzina, C. Ledford, T. Horn, P. Carriere, and P. Frigola, Design and test of copper printed rf cavities, in *Proceedings of the 2020 IEEE 21st International Conference on Vacuum Electronics (IVEC), Monterey, CA* (IEEE, New York, 2020), pp. 149–150, 10.1109/IVEC45766.2020.9520624.

[13] M. Mayerhofer, J. Mitteneder, and G. Dollinger, A 3D printed pure copper drift tube linac prototype, Rev. Sci. Instrum. **93**, 023304 (2022).

[14] M. Mayerhofer, S. Brenner, E. Chyhyrynets, M. Dickmann, V. Nedeljkovic-Groha, R. Helm, D. Heußen, J. Mitteneder, C. Pira, and G. Dollinger, Laser powder bed fusion for x-band rf cavities: A preliminary study, in *Proceedings of the 16th International Particle Accelerator Conference, Taipei, Taiwan* (JACoW, Geneva, Switzerland, 2025), pp. 2616–2619, 10.18429/JACOW-IPAC2025-THPB052.

[15] C. Zhang, R. Böhm, E. Boos, R. Cherif, A. Japs, and S. Wunderlich, From concept to reality: Additive manufacturing in particle accelerator and storage ring R&D at GSI and for FAIR, arXiv:2509.22397.

[16] M. Mayerhofer, H. Hähnel, G. Dollinger, J. Sonpar, and R. Helm, A novel test cavity setup for surface conductivity measurements of additive manufacturing samples, in *Proceedings of the 32nd Linear Accelerator Conference, LINAC-2024, Chicago, IL* (JACoW, Geneva, Switzerland, 2024), pp. 363–366, 10.18429/JACOW-LINAC2024-TUPB019.

[17] A. Seltzman and S. Wukitch, RF losses in selective laser melted GRCop-84 copper waveguide for an additively manufactured lower hybrid current drive launcher, Fusion Eng. Des. **159**, 111762 (2020).

[18] T. Torims, A. Cherif, N. Delerue, M. F. Pedretti, S. Gruber, D. Krogere, E. Lopez, T. Otto, G. Pikurs, M. Pozzi, A. Ratkus, M. Thielmann, M. Vedani, M. Vretenar, and P. Wagenblast, Evaluation of geometrical precision and surface roughness quality for the additively manufactured radio frequency quadrupole prototype, J. Phys. Conf. Ser. **2420**, 012089 (2023).

[19] P. Rebesan, V. Candela, S. Candela, R. Dima, E. Chyhyrynets, M. Bonesso, M. Pozzi, A. Pepato, D. Ford, C. Pira, and G. Favero, Additive manufacturing of 6 GHz seamless SRF copper cavities: Printing, surface treatments and performance investigations, in *Proceedings of the 14th International Particle Accelerator Conference, IPAC-2023, Venice, Italy* (JACoW, Geneva, Switzerland, 2023), pp. 4943–4946, 10.18429/JACOW-IPAC2023-THPM023.

[20] Q. M. Khan and D. Kuylenstierna, Analysis of Q-factor for AM-SLM cavity based resonators using surface roughness models, IEEE J. Multiscale Multiphys. Comput. Tech. **9**, 75 (2024).

[21] H. Hähnel, A. Ratkus, D. Benjamin, C. Pira, E. Chyhyrynets, M. Pozzi, M. Vedani, M. Vretenar, N. Kunkel, R. Caforio, T. Romano, and T. Torims, Surface finishing of additive manufacturing parts for particle accelerators, in *Proceedings of the 32nd Linear Accelerator Conference, LINAC-2024, Chicago, IL* (JACoW, Geneva, Switzerland, 2024), pp. 367–370, 10.18429/JACOW-LINAC2024-TUPB020.

[22] S. Gruber, L. Stepien, E. López, F. Brueckner, and C. Leyens, Physical and geometrical properties of additively manufactured pure copper samples using a green laser source, Materials **14**, 3642 (2021).

[23] Q. Jiang, P. Zhang, Z. Yu, H. Shi, D. Wu, H. Yan, X. Ye, Q. Lu, and Y. Tian, A review on additive manufacturing of pure copper, Coatings **11**, 740 (2021).

[24] S. Kurennoy, L. Rybarcyk, and T. Wangler, Efficient accelerating structures for low-energy light IONS, in *Proceedings of the 22nd Particle Accelerator Conference, PAC-2007, Albuquerque, NM* (IEEE, New York, 2007), pp. 3824–3826, 10.1109/PAC.2007.4439921.

[25] S. S. Kurennoy, L. J. Rybarcyk, J. F. O'Hara, E. R. Olivas, and T. P. Wangler, H-mode accelerating structures with permanent-magnet quadrupole beam focusing, Phys. Rev. ST Accel. Beams **15**, 090101 (2012).

[26] R. Tang, C. Du, X. Guan, Y. Lei, J. Li, P. Ma, K. Man, C. Tang, X. Wang, Q. Xing, W. Ye, H. Zhang, and S.-X. Zheng, Tuning and low power test of the 325 MHz IH-DTL at Tsinghua University, in Proceedings of the 29th Linear Accelerator Conf. (LINAC'18), Beijing, China (JACoW, Geneva, Switzerland, 2018), pp. 759–762, 10.18429/JACOW-LINAC2018-THPO035.

[27] P. Ma, R. Tang, Y. Yang, S. X. Zheng, W. B. Ye, M. W. Wang, W. L. Liu, B. C. Wang, Q. Z. Xing, C. T. Du, H. Y. Zhang, J. Li, X. L. Guan, X. W. Wang, Z. M. Wang, and M. T. Qiu, Development of a compact 325 MHz proton interdigital H-mode drift tube linac with high shunt impedance, Phys. Rev. Accel. Beams **24**, 020101 (2021).

[28] Y. Nakazawa, E. Cicek, K. Futatsukawa, Y. Fuwa, N. Hayashizaki, T. Iijima, H. Iinuma, Y. Iwata, Y. Kondo, T. Mibe, S. Mizobata, T. Morishita, M. Otani, Y. Sue, Y. Takeuchi, and J. Tojo, High-power test of an interdigital H-mode drift tube linac for the J-PARC muon $g-2$ and electric dipole moment experiment, Phys. Rev. Accel. Beams **25**, 110101 (2022).

[29] U. Ratzinger, H. Hähnel, R. Tiede, J. Kaiser, and A. Almomani, Combined zero degree structure beam dynamics and applications, Phys. Rev. Accel. Beams **22**, 114801 (2019).

[30] R. Tiede, G. Clemente, H. Podlech, U. Ratzinger, A. Sauer, and S. Minaev, LORASR code development, in *Proceedings of the 10th European Particle Accelerator Conference, Edinburgh, Scotland, 2006* (EPS-AG, Edinburgh, Scotland, 2006), pp. 2194–2196.

[31] R. Tiede, D. Mäder, N. F. Petry, H. Podlech, U. Ratzinger, and C. Zhang, Improvements of the LORASR code and their impact on current beam dynamics designs, in *Proceedings of the 27th International Conference, LINAC-2014, Geneva, Switzerland* (JACoW, Geneva, Switzerland, 2014), pp. 569–571.

[32] D. Uriot and N. Pichoff, Status of TraceWin code, in *Proceedings of the 6th International Particle Accelerator Conference, IPAC-2015, Richmond, VA* (JACoW, Geneva, Switzerland, 2015), 10.18429/JACOW-IPAC2015-MOPWA008.

[33] Dassault Systemes, SIMULIA CST Studio Suite (including CST Microwave Studio), Available at https://www.3ds.com/products/simulia/cst-studio-suite (2025).

[34] H. Hähnel, A. Ates, B. Dedic, C. Wagner, J. Kaiser, and U. Ratzinger, RF conditioning of an IH-DTL cavity made using additive manufacturing, in *Proceedings of the 15th International Particle Accelerator Conference, IPAC-2024, Nashville, TN* (JACoW, Geneva, Switzerland, 2024), pp. 3501–3504, 10.18429/JACOW-IPAC2024-THPR10.

[35] H. Hähnel, P. Müller, J. Kaiser, A. Ates, B. Dedic, U. Ratzinger, and C. Wagner, Further high power tests of the additive manufacturing IH-type cavity, in *Proceedings of the 16th International Particle Accelerator Conference, IPAC-2025, Taipei, Taiwan* (JACoW, Geneva, Switzerland, 2025), pp. 1666–1669, 10.18429/JACOW-IPAC2025-WEAD3.

[36] C. Wagner, A. Ates, and H. Hähnel, A hybrid LINAC low level rf control system for FRANZ, in *Proceedings of the 16th International Particle Accelerator Conference, IPAC-2025, Taipei, Taiwan* (JACoW, Geneva, Switzerland, 2025), pp. 3203–3205, 10.18429/JACOW-IPAC2025-THPS116.

[37] C. Wagner, A. Ates, and H. Hähnel, MNDACS—Mesh networked data acquisition and control system, in *Proceedings of the 16th International Particle Accelerator Conference, IPAC-2025, Taipei, Taiwan* (JACoW, Geneva, Switzerland, 2025), pp. 3200–3202, 10.18429/JACOW-IPAC2025-THPS115.

[38] J. Kaiser, A. Ates, and H. Hähnel, Development of a compact rf coupler utilizing additive manufacturing, in *Proceedings of 32nd Linear Accelerator Conference, LINAC-2024, Chicago, IL* (JACoW, Geneva, Switzerland, 2024), pp. 375–378, 10.18429/JACOW-LINAC2024-TUPB022.

[39] J. F. Ziegler, SRIM—The stopping and range of ions in matter, Available at http://www.srim.org (2013) [accessed August 2025].

[40] National Institute of Standards and Technology (NIST), Pstar: Stopping power and range tables for protons, Available at https://physics.nist.gov/PhysRefData/Star/Text/PSTAR.html [accessed August 2025].

[41] Mesytec GmbH & Co. KG, Mesytec—Detector readout systems (2025), https://www.mesytec.com/ [accessed October 27, 2025].

[42] T. Heftrich (private communication).

[43] M. Mayerhofer, A. Bergmaier, G. Datzmann, H. Hagn, R. Helm, J. Mitteneder, R. Schubert, L. Picardi, P. Nenzi, C. Ronsivalle, H.-F. Wirth, and G. Dollinger, Concept and performance evaluation of two 3 GHz buncher units optimizing the dose rate of a novel preclinical proton minibeam irradiation facility, PLoS One **16**, e0258477 (2021).